2 Fabry–Perot Lasers: Temperature and Many-Body Effects

B. Grote[1], E. K. Heller[1], R. Scarmozzino[1], J. Hader[2], J. V. Moloney[2], and S. W. Koch[3]

[1] RSoft Design Group, 200 Executive Blvd, Ossining, New York 10562, bernhard_grote@rsoftdesign.com
[2] Arizona Center for Mathematical Sciences, University of Arizona, Tucson, Arizona 85721, jhader@dinha.acms.arizona.edu
[3] Physics Department and Material Sciences Center, University of Marburg, Renthof 5, 35037 Marburg, Germany

2.1 Introduction

In this chapter, we demonstrate the integration of microscopic gain modeling into the laser design tool LaserMOD, which is derived from the Minilase II simulator developed at the University of Illinois [1]. Multidimensional carrier transport, interaction with the optical field via stimulated and spontaneous emission, as well as the optical field are computed self-consistently in our full-scale laser simulations. Giving additional details with respect to our previous work [2], we demonstrate the effectiveness of this approach by investigating the temperature sensitivity of a broad-ridge Fabry–Perot laser structure with InGaAsP multi-quantum wells for 1.55 μm emission wavelength.

Monochromatic light sources are key components in optical telecommunication systems. Predominantly, this need has been filled by semiconductor lasers due to their narrow linewidth. However, increasingly stringent requirements for bandwidth, tunability, power dissipation, temperature stability, and noise are being placed on these devices to meet network demands for higher capacity and lower bit error rates. As in the semiconductor industry, where electronic design automation assists in designing multimillion-gate integrated circuits, it is becoming common practice to employ simulation tools for designing and optimizing telecommunication networks and components. As a consequence of predictive modeling, the time to market as well as development cost of telecommunication infrastructure can be reduced, as fewer cycles between design and experimental verification are necessary.

Different levels of model abstraction are used to describe the behavior of devices, depending on whether they are being simulated alone or with other components in an optical system. At the lowest level, simulations treat the fundamental device physics rigorously, whereas behavioral modeling, which allows for an increased number of elements to be treated, is applied at the system or network level. This chapter will focus on the former approach.

To predict the performance of a new design, a successful commercial laser simulator must account for the many complex physical processes that con-

tribute to the device operation. Mainly, the optical field and its interactions with the carrier populations must be described self-consistently, as they are strongly coupled via radiative recombination.

Classic approaches for solving the carrier and energy transport equations, such as drift-diffusion, heat flow, and energy balance equations, have been well established by the silicon device simulation industry [3–10]. Historically, the drift-diffusion model constitutes the first approach developed for semiconductor device simulation [3]. Within a momentum expansion of Boltzmann's transport equations, the charge conservation represents only the lowest order contribution. The hydrodynamic and energy balance models include differential equations describing the conservation of momentum and energy [5, 6]. From this system of equations, the drift-diffusion equations can be obtained by assuming constant and equal temperatures for electrons, holes, and the crystal lattice. The thermodynamic model applies principles of irreversible thermodynamics and linear transport theory to derive a system of equations describing carrier concentrations as well as carrier and lattice temperatures [9, 11]. It can be shown that the thermodynamic and the hydrodynamic approaches result in equivalent equations for the thermal transport [12, 13].

However, aside from the simulation of electronic transport within a classic framework, lasers also require quantum mechanical methods to treat light emission and amplification. These theoretical modeling techniques are far less mature. Specifically, bound quantum well states that give rise to lasing transitions must be modeled quantum mechanically; yet they must also be coupled to the classically modeled propagating states that describe the electronic transport. Progress has been made in this area by employing rate equations to describe carrier capture and scattering between classic propagating states and bound quantum well states [1, 14].

Optical gain/absorption and spontaneous emission or photoluminescence couple transport and optics in optoelectronic devices, as they correlate the complex refractive index with radiative recombination and generation of carriers. In lasers, strong coupling occurs due to stimulated emission. Methodologies for treating the optical aspect of the coupled problem are based on different proven approaches of solving Maxwell's equations. Gain/absorption and photoluminescence are determined by the energetic position and oscillator strength of optical transitions. The optical transitions in a semiconductor quantum well depend on the detailed bandstructure, which has to be calculated for the given geometry and material composition of quantum well and barrier. $\mathbf{k} \cdot \mathbf{p}$-perturbation theory has been widely adopted to compute the electron and hole energy dispersion, the optical transition matrix elements, the subband levels, and the confinement wavefunctions based on the knowledge of the bulk bandstructure [15–22].

In free-carrier or oscillator model approaches, interactions between the carriers are neglected and analytic expressions for the gain can be obtained based on Fermi's Golden Rule or by deriving equations of motion from the

corresponding system Hamiltonian of a noninteracting electron gas or two-level system, respectively. Carrier collision effects are introduced phenomenologically in terms of a lineshape function that has a width determined by an effective decay rate [23, 24]. These kinds of models are often employed in laser simulation tools, as their simplicity allows us to avoid the excessive computational effort imposed by the full treatment of carrier interactions, which requires making the Hamiltonian diagonal with respect to the quasi-particle interactions.

However, it has been shown that accurate modeling of gain and absorption spectra requires the accounting of many-body interactions, leading to effects such as Coulomb enhancement, excitonic correlation, and band gap renormalization. In Chapt. 1, "Gain and Absorption: Many-Body Effects" by S. W. Koch et al., a discussion of many-body effects and the underlying theory can be found. In Sect. 3.1 of Chapt.1 and Fig. 2 within that section, the free-carrier gain model is compared with the full many-body calculation and experimental gain spectra. It can be seen that, for a series of measurements, such as the density-dependent set of gain spectra shown in Fig. 2 of Chapt. 1, satisfying agreement between theory and experiment can only be achieved by taking into account many-body effects. For low carrier densities and temperatures, the absorption of semiconductors around the bandedge is dominated by a pronounced exciton resonance. These electron–hole correlations persist even for higher densities and temperatures and influence the spectra beyond the effects due to band gap renormalizations alone. Furthermore, dephasing by carrier–carrier and carrier–phonon scattering can lead to a broadening energy of the spectra. It is clear that reliable prediction of the density and temperature dependence of such spectral characteristics as the energetic position, broadening, and oscillator strength of optical transitions requires that all significant interactions are taken into account (see, e.g., [25–27]). In the many-body gain model employed here, real and imaginary parts of eigenenergy renormalizations describe band gap and excitonic shifts as well as collision broadening. These effects are not treated phenomenologically, but within the framework of a quantum kinetic theory that rigorously treats the Coulomb interaction in system Hamiltonian for electrons and holes [25, 26].

In the phenomenological treatment, a gain model would require the user to specify energetic shift and broadening parameters. This prohibits the prediction of absolute magnitude and shape of the gain over a range of temperatures and densities for a specific material system. Although several experimental behaviors of laser devices can be described by the phenomenological effective decay rate treatment, it cannot reproduce certain experimental features in the gain spectra that are important for advanced laser structures. It has been shown that the accurate description of gain and absorption spectra, in the neighborhood of the transparency carrier density and over a variety of carrier densities and temperatures, requires the full treatment of carrier interactions. Section 3.3 of Chapt. 1 discusses the dephasing-time approach

and its limitations. Approximate results are compared to gain spectra obtained employing the full many-body calculation including scattering terms and to experimental findings. Without the predictive knowledge, calibration of gain parameters might imply additional iterations between simulation and experimental verification during the laser design process, increasing effort in cost and time.

A completely microscopic treatment, alternatively, does not require any experimentally measured fitting parameters such as lineshape broadenings or spectral shifts. It can quantitatively predict the absorption, gain, and photoluminescence spectra of ideal structures using only basic bandstructure parameters, which are independent of carrier density, temperature, and the design of the quantum well. Real samples are usually affected by a certain amount of disorder. In semiconductor quantum wells, crystal inhomogeneities, such as local well width fluctuations or local fluctuations of the material composition, lead to an inhomogeneous broadening of spectra in addition to the homogeneous broadening due to electron–electron and electron–phonon scattering. Moreover, magnitude of fluctuations, as well as average material composition and sample geometry, can vary across the wafer. The results of a simple low-excitation photoluminescence measurement performed directly on the wafer for the nonideal sample may be compared with predictions of the microscopic theory for the ideal structure. This allows for the determination of the inhomogeneous broadening, as well as possible deviations between nominal and actual structural parameters, which are all independent of carrier density and temperature. This method has recently received attention for application as an on-wafer testing tool [28, 29]. Once the amount of disorder has been characterized, the theory is completely parameter free and can predict the optical properties for the device under high excitation operating conditions.

In a rigorous laser simulation, the overall complexity of treating the coupled transport and optoelectronic problem leads to significant computational effort. In practice, a number of approximations have to be made in order to produce a more tractable simulation. Complexity is reduced with respect to the full microscopic description, at the expense of some predictability, by relying on careful calibration of model parameters introduced through a phenomenological treatment. A good phenomenological model requires only a few parameters that need calibration, while preserving the basic functional dependencies given by the microscopic theory. This concept is very common in semiconductor device and laser simulation where many processes involved in the carrier transport have to be described. However, it is important to identify the most critical processes, where enhancements in the level of accuracy can improve the quality of the result of the overall simulation with acceptable increase of computational effort.

The microscopic many-body theory of the gain employed by our simulator allows us to re-examine the underlying approximation of noninteracting particles leading to the simpler free-carrier gain model with phenomenolog-

ical broadening parameter as well as the trade-off between computational effort and predictability. The rigorous microscopic many-body theory of the semiconductor, which is based on the semiconductor Bloch equations, allows for the accurate modeling of the spectral characteristics of the material gain. With such a model, the energetic position of the gain peak, the broadening due to quasi-particle collisions, and therefore, the absolute magnitude of the gain can be predicted based solely on fundamental bulk material parameters. The properties of the gain are found to be the most critical contributions to the overall slope efficiency, threshold current, and emission wavelength of the laser. By comparing computations with experimental results, we will show, that the use of the advanced gain model can improve the overall predictability of the simulator.

We note that significant computational effort is associated with the quantum many-body gain calculation. In order to avoid the gain calculation during full-scale laser simulations, which can be numerous in design optimization cycles, the gain and related quantities, such as refractive index change and photoluminescence, are precomputed and stored as a data base. For different common material systems associated with specific telecommunication laser emission wavelength, the creation of libraries, which are parameterized by material composition and quantum well geometry, might be attractive. During a full-scale laser simulation the gain, refractive index, and photoluminescence data can be retrieved from the precomputed spectra for the current operating condition, to perform self-consistent computations of optical field, carrier transport, and their interactions to obtain steady-state, transient, or frequency responses for a particular laser geometry. Taking advantage of this methodology, computation times for the full-scale laser simulation using the many-body gain model are comparable with or even faster than those using a run-time gain calculation based on the free-carrier approach.

In Sect. 2.2 we describe the theoretical background of the transport, optical, and optoelectronic modeling applied in our simulator. The temperature sensitivity of an InGaAsP multi-quantum well laser is analyzed in Sect. 2.3 using the many-body gain theory in comparison to the free-carrier gain model. Our findings are summarized in Sect. 2.4.

2.2 Theory

2.2.1 Transport

A methodology for the carrier transport has been developed and established for silicon device simulation in multiple dimensions, which we adapt for material systems common to semiconductor lasers, to describe electronic transport through bulk regions, in which active layers may be embedded [10, 11]. The injection current into the active quantum well region determines the

Table 2.1. Nomenclature.

Symbol	Definition
B	Einstein coefficient
$C_{e/h}^{Auger}$	electron/hole Auger recombination coefficient
c	vacuum speed of light
c_L	crystal lattice heat capacity
$E_{e/h}^{Auger,act}$	Auger recombination activation energy
$F_{e/h}$	electron/hole Fermi level
$f_{e/h}$	electron/hole distribution functions
$f_{e/h}^{2D/3D}$	quantum well electron/hole distribution function for propagating/bound states
$G(\omega)$	gain spectrum
$G_{thermal}$	lumped thermal conductivity
$g_{e/h}^{3D/2D}$	density of states for quantum well propagating/bound states
H	total heat generation rate
H_{Joule}	Joule heat source
H_{rec}	recombination heat source
H_{trans}	heat source due to transient modulation of carrier concentrations
$H_{Peltier+Thomson}$	sum of Peltier and Thomson heat sources
$\mathbf{J}_{e/h}$	electron/hole current
k_B	Boltzmann constant
k_0	wavenumber for Helmholtz equation
$k_{e/h}^{fca}$	free-carrier absorption coefficients for electrons/holes
$\mathcal{L}_{i,j}$	Lorentzian broadening around transition frequency $\omega_{i,j}$
q	elementary charge
$N_{D/A}^{\pm}$	ionized donors/acceptors
$n_{e/h}$, $n_{e/h}^{3D}$, $n_{e/h}^{2D}$, $n_{e/h}^{2D,i}$	electron/hole concentrations, total propagating ($3D$) and bound ($2D$) quantum well densities, individual subband (i) contributions for bound states
n_i	intrinsic carrier density
$n_{e/h}^{t}$	electron/hole trapped carrier density
n_{ph}	phonon density
$n_{eff,\nu}$	effective index as given by eigenvalue ν of the Helmholtz equation
$P_{e/h}$	electron/hole thermoelectric power
R_{dark}, R_{Auger}, R_{SRH}	total nonradiative, Auger and Shockley–Read–Hall recombination
R_{stim}, $R_{spon,bound/bulk}$	stimulated and spontaneous recombination for bound/bulk states
$R_{capture}^{e/h}$, $R_{capture,cc/ph}^{e/h}$	electron/hole quantum well net capture rate, contribution due to carrier–carrier/carrier–phonon scattering
$s_{e/h}^{capture/escape,cc/ph}$	electron/hole capture/escape coefficient for carrier–carrier/carrier–phonon scattering
$\mathcal{S}_{\nu,\omega}$	photon occupation of mode (ν, ω)
$\mathbf{S}_{e/h}$	electron/hole energy flux
T, T_C	temperature, contact temperature
t	time
$U(\omega)$	spontaneous emission spectrum
$Z(\omega)$	photon density of states
α_0	background absorptive loss (carrier independent)
ϵ	static dielectric permittivity
Φ	electric potential
γ_0, γ_{inh}	homogeneous, inhomogeneous broadening
$\kappa_{L/e/h}$	crystal lattice/electron gas/hole gas heat conductivity
$\tau_{e/h}^{SRH}$	Shockley–Read–Hall electron/hole lifetime
$\tau_{\nu,\omega}^{photon}$, τ_{mirror}, $\tau_{scatter}$	total photon losses, mirror losses, scatter losses
ω_{LO}	longitudinal optical phonon frequency
$\psi_i^{e/h}$	quantum well confinement wavefunction of subband i
ζ_ν	νth Helmholtz eigenmode

carrier densities within bound quantum well states and, therefore, the degree of inversion. For carrier transport through bulk semiconductor regions, the drift-diffusion system of equations is applied. The electric potential ϕ is determined by Poisson's equation,

$$\nabla \cdot \epsilon \nabla \phi = q(n_e - n_h - N_D^+ + N_A^-), \tag{2.1}$$

where the charges are given by the densities of electrons n_e, holes n_h, ionized donors N_D^+, and acceptors N_A^- (q is the elementary charge and ϵ is the static dielectric permittivity of the respective material). A list of symbols used in this chapter and their definition can by found in Table 2.1. For quantum wells, we distinguish between carriers in propagating ($n_{e/h}^{3D}$) and bound states ($n_{e/h}^{2D}$). Although all states are considered propagating in bulk regions ($n_{e/h}^{2D} = 0$), the confinement potential leads to bound states localized within the quantum well. Within an envelope function approximation, the spatial distribution of carriers in the confined direction of the quantum well is described by wavefunctions, which are obtained by solving the Schroedinger equation for the potential given by the solution of Poisson's equation and the band gap offsets. With wavefunctions $\psi_i^{e/h}$ for subband i, the spatial distribution of bound electrons and holes (indicated by indices e/h) in the direction perpendicular to the quantum well plane is given by:

$$n_{e/h}^{2D}(\mathbf{r}) = \sum_i |\psi_i^{e/h}(y)|^2 n_{e/h}^{2D,i}(\mathbf{r}_\parallel). \tag{2.2}$$

Here, y denotes the growth direction and coordinates perpendicular to the y-axis and parallel to the quantum well plane are indicated by $\parallel$. Light propagation within the Fabry–Perot cavity is assumed to be along the z-axis. The carrier density $n_{e/h}^{2D,i}$ in subband i is related to the distribution function $f_{e/h}^{2D}$ via the density of states $g_{e/h}^{2D,i}$,

$$n_{e/h}^{2D,i} = \int_{E_i}^{\infty} g_{e/h}^{2D,i}(E) f_{e/h}^{2D,i}(E), \tag{2.3}$$

which results from our eight band $\mathbf{k} \cdot \mathbf{p}$ calculation. The total charge due to electrons is given by the sum over bound and propagating contributions, $n_{e/h} = n_{e/h}^{3D} + n_{e/h}^{2D}$.

Figure 2.1 illustrates our transport model applied to quantum well regions. Capture due to carrier–carrier and carrier–phonon scattering couples the classic propagating bulk and quantum well continuum states to the quantum confined bound states. The corresponding rates enter the continuity equations for carriers in bound and continuum states [1, 30]. Carriers entering the quantum well in continuum states can transit through or get captured into bound states as a result of scattering events involving other carriers or phonons. For sufficiently fast inter-subband scattering leading to thermalization between

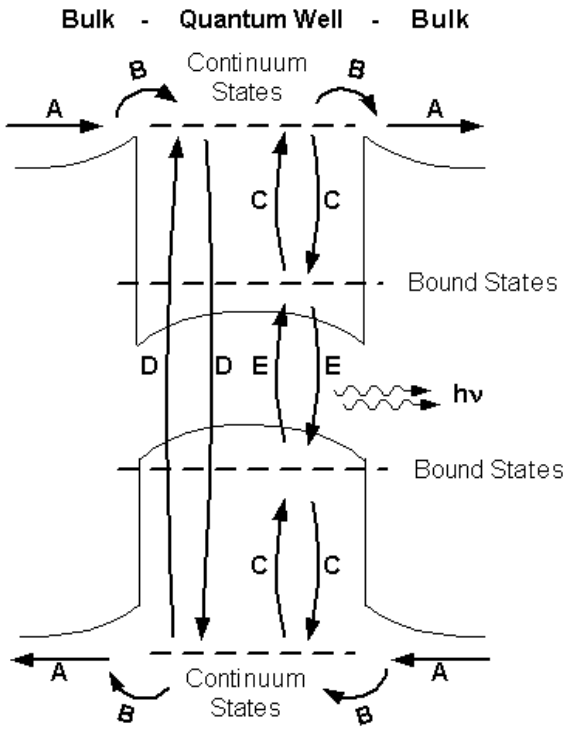

Fig. 2.1. Schematic illustration of the transport model applied to quantum well regions including drift-diffusion currents in bulk regions (A), transport across interfaces (B), carrier capture from continuum into bound states (C), radiative and nonradiative recombination from bound states (E), and nonradiative recombination from continuum states or for bulk carriers (D) (from [2]).

the subbands, the occupation of bound states can be described by a single Fermi level. This reduces the set of rate equations in the quantum wells to a four-level system defined by effective rates and density of states, which are the sum over individual subband contributions $f_{e/h}^{2D,i} = f_{e/h}^{2D}$, $g_{e/h}^{2D} = \sum_i g_{e/h}^{2D,i}$. The total bound carrier concentration is described by a continuity equation:

$$\frac{\partial n_{e/h}^{2D}}{\partial t} = \pm\frac{1}{q}\nabla_{\parallel} \cdot \mathbf{J}_{e/h\,\parallel} - R_{dark} - R_{stim} - R_{spon,bound} + R_{capture}^{e/h}. \quad (2.4)$$

Via the capture rate $R_{capture}^{e/h}$, the bound carriers couple to the continuum concentrations, where it enters the continuity equation as a loss:

$$\frac{\partial n_{e/h}^{3D}}{\partial t} = \pm\frac{1}{q}\nabla \cdot \mathbf{J}_{e/h} - R_{dark} - R_{spon,bulk} - R_{capture}^{e/h}. \quad (2.5)$$

Capture into and escape from bound states is modeled by Master equation type rates for in- and out-scattering due to carrier–carrier and carrier–phonon interaction. The net capture rate $R^{e/h}_{capture} = R^{e/h}_{capture,cc} + R^{e/h}_{capture,ph}$ is given by:

$$\begin{aligned} R^{e/h}_{capture,cc} = \int_{E^0_{e/h}}^{\infty} dE \int_{E^0_{e/h}}^{\infty} dE' g^{3D}_{e/h}(E)\, g^{2D}_{e/h}(E') \times \\ \times \; \big(s^{cc,capture}_{e/h}(E,E')\, f^{3D}_{e/h}(E)\, (1 - f^{2D}_{e/h}(E')) \\ - \; s^{cc,escape}_{e/h}(E,E')\, (1 - f^{3D}_{e/h}(E))\, f^{2D}_{e/h}(E') \big), \end{aligned} \tag{2.6}$$

describing carrier–carrier scattering, and:

$$\begin{aligned} R^{e/h}_{capture,ph} = \int_{E^0_{e/h}}^{\infty} dE \int_{E^0_{e/h}}^{\infty} dE' g^{3D}_{e/h}(E)\, g^{2D}_{e/h}(E') \times \\ \times \; \big(s^{ph,capture}_{e/h}(E,E')\, (n_{ph}+1)\, f^{3D}_{e/h}(E)\, (1 - f^{2D}_{e/h}(E')) \\ - \; s^{ph,escape}_{e/h}(E,E')\, n_{ph}\, (1 - f^{3D}_{e/h}(E))\, f^{2D}_{e/h}(E') \big), \end{aligned} \tag{2.7}$$

modeling scattering of carriers with longitudinal optical phonons. In general, the scattering coefficients $s^{cc/ph,capture/escape}_{e/h}$ would have to be assumed to be dependent on the occupation of the involved states to emulate the dynamics of the quantum Boltzmann equation used for the microscopic description of the scattering process. Following [1], the scattering coefficients are given by constant rates normalized by the final density of states. In (2.7), absorption or emission of longitudinal optical phonons allows for interaction of energetically nonresonant states by transfer of a phonon energy. The phonon occupation is assumed to be [1]:

$$n_{ph} = \frac{1}{\exp(\frac{\hbar\omega_{LO}}{k_B T}) - 1}, \tag{2.8}$$

with longitudinal optical phonon energy $\hbar\omega_{LO}$, Boltzmann constant k_B, and temperature T. We assume energy conservation within the electron gas under elastic carrier–carrier scattering described by (2.6).

The net recombination rate $R_{dark} = R_{SRH} + R_{Auger}$ balances recombination and generation due to nonradiative processes, such as Auger recombination:

$$R_{Auger} = (C^{Auger}_h n_h + C^{Auger}_e n_e)(n_e n_h - n_i^2), \tag{2.9}$$

and Shockley–Read–Hall recombination:

$$R_{SRH} = \frac{n_e n_h - n_i^2}{\tau^{SRH}_h (n_e + n^t_e) + \tau^{SRH}_e (n_h + n^t_h)}. \tag{2.10}$$

Here, n_i is the intrinsic carrier density, $n^t_{e/h}$ are the respective trapped carrier densities, $\tau^{SRH}_{e/h}$ are the lifetimes of electrons and holes for trap-assisted

recombination, and $C_{e/h}^{Auger}$ in (2.9) are the coefficients for the electron and hole Auger process. The temperature dependence of the Auger recombination can be modeled by [31, 32]:

$$C_{e/h}^{Auger}(T) = C_{e/h}^{Auger}(300\ \mathrm{K}) \exp\big(-\mathrm{E}_{\mathrm{e/h}}^{\mathrm{Auger,act}}(\frac{1}{\mathrm{k_B T}} - \frac{1}{\mathrm{k_B} 300\ \mathrm{K}})\big), \quad (2.11)$$

with activation energies $E_{e/h}^{Auger,act}$. Nonradiative processes, as well as spontaneous emission into modes other than the lasing modes, decrease the carrier densities without contributing to the laser output power.

Aside from nonradiative recombination, stimulated and spontaneous emission lead to a decrease of the carrier population within bound quantum well states. The spontaneous emission is given by:

$$R_{spon,bound} = \int d\omega Z(\omega) U(\omega), \quad (2.12)$$

where ω is the angular frequency, $Z(\omega)$ is the spectral density of photon states, and U is the photoluminescence spectrum. The recombination due to stimulated emission,

$$R_{stim} = \sum_{\nu,\omega} \mathcal{S}_{\nu,\omega} |\zeta_\nu|^2 \frac{c}{n_{eff,\nu}} G(\omega), \quad (2.13)$$

is the sum over light emission into all Fabry–Perot modes denoted by ω and eigenmodes ζ_ν of the plane perpendicular to the light propagation. G is the gain spectrum as given by the interband transitions of the quantum well. Eigenmodes and effective refractive indices $n_{eff,\nu}$ are determined by the solution of a Helmholtz eigenvalue problem. c is the speed of light. The photon occupation number $\mathcal{S}_{\nu,\omega}$ obeys a rate equation (see Sect. 2.2.2). In bulk regions and for continuum states, a simplified model is applied to account for recombination due to spontaneous emission:

$$R_{spon,bulk} = B(n_e n_h - n_i^2), \quad (2.14)$$

where B is the spontaneous recombination coefficient.

The current densities $\mathbf{J}_{e/h}$ are calculated within the framework of the drift-diffusion theory. For Fermi statistics, the diffusivity is related to the carrier mobility by a generalized Einstein relation. Transport across material interfaces constituting a bandedge discontinuity is described in terms of thermionic emission. Within the quantum well plane, indicated by $\|$, continuum and bound carriers can drift leading to injection losses due to lateral leakage currents, see (2.4). For bulk regions, (2.5) reduces to the well-known continuity equations for electrons and holes, as all states are considered propagating.

Due to carrier–phonon scattering, part of the electronic energy is transferred to the crystal lattice resulting in an increase of the lattice temperature.

Instead of deriving quantum mechanical equations of motion for the phonon population interacting with electrons and holes, classic thermal transport equations, which describe the average energy of the respective subsystems of electrons, holes, and host lattice, are typically employed in device simulation drastically reducing the problem complexity [5–11, 33]. In semiconductor laser diodes, self-heating under continuous-wave (CW) operation is known to affect the characteristics significantly and often limits the performance, as recombination and transport processes explicitly or implicitly depend on the temperature. In order to model these effects, a lattice heat flow equation has to be solved to determine the temperature profile within the device [9, 34]:

$$\left(c_L + \frac{3}{2}k_B(n_e + n_h)\right)\frac{\partial T}{\partial t} = \nabla \cdot \left(\kappa_L \nabla T - \mathbf{S}_e - \mathbf{S}_h\right) + H. \tag{2.15}$$

Here, c_L is the heat capacity of the lattice and κ_L is the lattice thermal conductivity. The energy fluxes $\mathbf{S}_{e/h}$ are given by:

$$\mathbf{S}_{e/h} = \mp P_{e/h} T \mathbf{J}_{e/h} - \kappa_{e/h} \nabla T, \tag{2.16}$$

with thermoelectric powers $P_{e/h}$ and thermal conductivity mediated by electrons and holes $\kappa_{e/h}$. Including contributions due to temperature gradients, the current densities are given by:

$$\mathbf{J}_{e/h} = n_{e/h}\mu_{e/h}\left(\nabla F_{e/h} \pm q P_{e/h} \nabla T\right), \tag{2.17}$$

where $\mu_{e/h}$ are the mobilities and $F_{e/h}$ are the Fermi levels of electrons and holes, respectively. For the derivation of (2.15), the electron and hole temperature were assumed to be equal to the lattice temperature. The heat capacity and conductivities of the electron and hole gas add to the thermal properties of the lattice, as can be seen from the heat capacity term on the left-hand side of (2.15) as well as the heat flux term on the right-hand side. Heat generation $H = H_{Joule} + H_{rec} + H_{trans}$ in (2.15) is due to Joule heat:

$$H_{Joule} = -\frac{1}{q}\left(\mathbf{J}_e \cdot \nabla F_e + \mathbf{J}_h \cdot \nabla F_h\right), \tag{2.18}$$

recombination heat expressed by:

$$H_{rec} = (F_e - F_h) R_{dark}, \tag{2.19}$$

and an additional heat production rate originating from the transient modulation of the carrier concentrations:

$$H_{trans} = -T\frac{\partial F_e}{\partial T}\frac{\partial n_e}{\partial t} + T\frac{\partial F_h}{\partial T}\frac{\partial n_h}{\partial t}. \tag{2.20}$$

The sum of Peltier and Thomson heat:

$$H_{Peltier+Thomson} = -\mathbf{J}_e \cdot T\nabla P_e - \mathbf{J}_h \cdot T\nabla P_h, \tag{2.21}$$

is included in the convective part of the energy fluxes (see 2.16 and 2.15). The recombination heat source accounts for the energy of the order of the band gap dissipated to the lattice by nonradiative recombination. Note that radiative processes transfer this energy to the light field and, therefore, should not be included here.

Two different thermal contact models are common in physical device simulation. By assuming an isothermal contact with given temperature T_C, a Dirichlet boundary condition is imposed:

$$T = T_C. \tag{2.22}$$

The second model is of Cauchy type. It associates a finite thermal conductance $G_{thermal}$ with the contact to determine the heat flux through the contact area [35]:

$$-\kappa_L \mathbf{n} \cdot \nabla T = \frac{G_{thermal}}{A}(T - T_C), \tag{2.23}$$

where $\mathbf{n}$ is the surface normal vector at the contact and A is the contact surface area.

2.2.2 Optics

The light propagation within a waveguide structure is determined by the solution of Maxwell's equations. A set of approximations has been developed that reduces the computational effort with respect to the full solution for specific cavity structures. For Fabry–Perot lasers, the lateral modes can be described by a Helmholtz equation, whereas the resonator modes determine the spectrum of the axial direction. Photon rate equations describe the light intensity within the individual eigenmodes. Modal gain and spontaneous emission compensate losses due to different scattering and absorption mechanisms.

The waveguide properties of the semiconductor lasers are expressed by a Helmholtz eigenvalue equation describing stationary solutions of Maxwell's equations:

$$\left(\nabla_{x,y}^2 + k_0^2(n_b^2 - n_{eff,\nu}^2)\right)\zeta_\nu(x,y) = 0. \tag{2.24}$$

Here, n_b is the background refractive index, and k_0 is equal to ω/c with the angular frequency ω. The eigenvalues $n_{eff,\nu}$ determine the propagation along the optical z axis of the Fabry–Perot cavity:

$$\zeta_\nu(\mathbf{r}) = \zeta_\nu(x,y)\exp(\mathrm{i}n_{eff,\nu}k_0 z). \tag{2.25}$$

The mode profile is updated by solving (2.24) during the simulation to reflect index changes in the active layer. The light intensity within the different modes is determined by a set of photon rate equations:

$$\frac{\partial}{\partial t}\mathcal{S}_{\nu,\omega} = (G_{\nu,\omega} - \frac{1}{\tau_{\nu,\omega}^{photon}})\mathcal{S}_{\nu,\omega} + U_{\nu,\omega}. \tag{2.26}$$

Via the modal gain,

$$G_{\nu,\omega} = \int dV |\zeta_\nu|^2 \frac{c}{n_{eff,\nu}} G, \tag{2.27}$$

and the spontaneous emission,

$$U_{\nu,\omega} = \int dV |\zeta_\nu|^2 U, \tag{2.28}$$

electronic transport and optical properties are coupled. The losses,

$$\frac{1}{\tau_{\nu,\omega}^{photon}} = \frac{1}{\tau_{mirror}} + \frac{1}{\tau_{scatter}} + \frac{c}{n_{eff,\nu}} \alpha_b, \tag{2.29}$$

entering (2.26) are the sum of losses due to light leaving the cavity through the facets (τ_{mirror}), light scattered out of the waveguide ($\tau_{scatter}$), and absorptive losses (α_b). For narrow ridge waveguides, scatter losses can become considerable due to surface imperfections. Substantial losses due to intervalence band absorption in InGaAsP materials have been reported [32]. The absorptive losses α_b include free-carrier absorption mechanisms such as intervalence band absorption, which are modeled as being proportional to the carrier densities:

$$\alpha_b = \int dV |\zeta_\nu|^2 \left(k_e^{fca} n_e + k_h^{fca} n_h + \alpha_0 \right), \tag{2.30}$$

with free-carrier absorption coefficients $k_{e/h}^{fca}$ (α_0 accounts for carrier-independent background absorptive losses). Usually, barrier and other layer materials in semiconductor quantum well lasers are designed to be transparent at the laser wavelength given by the effective quantum well band gap. However, although band-to-band absorption may vanish, absorption spectra usually exhibit an Urbach tail due to phonon-assisted absorption and disorder-induced localized states below the band gap, contributing to background losses.

2.2.3 Gain

By coupling the electronic and optical subsystems, the spontaneous and, especially, the stimulated emission play a crucial role in the laser simulation. The gain computation for semiconductor quantum well lasers involves determining the bandstructure via methods such as $\mathbf{k} \cdot \mathbf{p}$ calculation and computing the subband spectrum to obtain optical matrix elements and density of states. Within the framework of a free-carrier approach, a noninteracting electron gas is assumed, allowing for the derivation of analytical expressions for gain and spontaneous emission. Broadening mechanisms are introduced via a phenomenological linewidth broadening function. In contrast, the many-body theory microscopically accounts for the effects of carrier–carrier interaction, including excitonic correlations as well as carrier–phonon scattering. The predictive capabilities of this method in determining the material gain spectra for a variety of materials has been proven in several publications [25, 27, 29].

2.2.3.1 Free-Carrier Gain Model

Neglecting interactions of carriers with other quasi-particles of the semiconductor, the gain G and spontaneous emission spectra U can be expressed as:

$$G = \int_0^\infty dE \sum_{i,j} \langle \psi_i^e | \psi_j^h \rangle \, (Bg_{red})_{i,j} \, (f_e^{2D} + f_h^{2D} - 1) \, \mathcal{L}_{i,j} \tag{2.31}$$

$$U = \int_0^\infty dE \sum_{i,j} \langle \psi_i^e | \psi_j^h \rangle (Bg_{red})_{i,j} \, f_e^{2D} \, f_{2D}^h \, \mathcal{L}_{i,j}. \tag{2.32}$$

Here, $\langle \psi_i^e | \psi_j^h \rangle$ is the overlap integral for the optical transition involving subbands i, j. The optical matrix element $(Bg_{red})_{i,j}$ is the product of Einstein coefficient and the reduced density of states, which results from our eight-band $\mathbf{k} \cdot \mathbf{p}$ bandstructure calculation. The range of integration includes all relevant transitions. The collision broadening term is modeled by a Lorentzian:

$$\mathcal{L}_{i,j}(E) = \frac{\gamma_0 / 2\pi}{(\hbar\omega_{i,j} - E)^2 + (\gamma_0/2)^2} \tag{2.33}$$

around the transition frequency $\omega_{i,j}$ and with the full-width half-maximum of γ_0.

2.2.3.2 Many-Body Gain Theory

The microscopic calculation of gain/absorption, refractive index, and photoluminescence spectra is described in detail in Chapt. 1, [25, 36], and references therein. It is based on solving the semiconductor Bloch equations, i.e., the equations of motion for the reduced density matrix, which are derived from the system Hamiltonian, including Coulomb interaction between carriers and carrier–phonon interaction. Consequently, Coulomb-induced effects like band gap renormalization, Coulomb enhancement of the absorption, and excitonic resonances are taken into account self-consistently. The electron–electron and electron–phonon scattering processes that lead to the dephasing of the polarizations and, therefore, spectral broadening and spectral shifts are calculated in second Born approximation. The resulting scattering equations take the form of generalized quantum-Boltzmann equations.

The diagonal elements of the reduced density matrix are the distribution functions, whereas the off-diagonal elements are the microscopic polarizations. The resulting polarizations are added up to the total macroscopic optical polarization, from which the optical susceptibility can be obtained through a simple Fourier transform. The real part of the susceptibility gives the carrier-induced change of the refractive index, and the imaginary part gives the gain/absorption. The photoluminescence spectra are derived from the absorption/gain spectra using the Kubo–Martin–Schwinger relation [37].

Spectra of gain, spontaneous emission, and carrier-induced change of the refractive index are precalculated and stored for a sufficiently dense grid of carrier density and temperature points. The full-scale laser simulation accesses this data base and interpolates for the required bound carrier density, temperature, and wavelength. Derivatives with respect to internal variables used in the Newton–Raphson method, which is applied to the solution of the system of coupled differential equations, are evaluated numerically.

2.3 Temperature Sensitivity of InGaAsP Semiconductor Multi-Quantum Well Lasers

Semiconductor lasers based on the InGaAsP-InP material system have gained great attention because the band gap allows tuning into the $1.3\ \mu\mathrm{m} - 1.6\ \mu\mathrm{m}$ range of emission wavelength suitable for optical fibers. Their performance is known to be strongly temperature dependent [38]. However, from an application point of view, it is desirable to achieve high-temperature stability of laser diodes. The necessity of cost-intensive cooling can be avoided, while gaining tolerance with respect to thermal interaction and, therefore, increasing flexibility in terms of packaging and integration. In this context, the performance of InGaAsP lasers at elevated temperatures is of interest, especially with regard to threshold current and slope efficiency.

Different physical processes have been discussed with respect to their role in determining the temperature sensitivity of these lasers: Auger recombination [39, 40], intervalence band absorption [41], carrier leakage out of the active region [42], lateral current spreading [43], barrier absorption and spontaneous recombination [44], as well as gain reduction [45]. The self-consistent modeling of all of these mechanisms is required for a theoretical investigation of the temperature sensitivity. In the past, most theoretical studies have been performed based on simple gain models, such as the free-carrier model or the oscillator model, which describe collision effects phenomenologically in terms of a gain broadening parameter. We will show that temperature and carrier-density-induced collision broadening of the gain spectrum is a dominant factor influencing the temperature sensitivity [2]. Carrier–carrier and carrier–phonon scattering-induced gain broadening can only be accounted for correctly by employing a theory that takes these many-body interactions into account self-consistently. We will point out shortcomings in phenomenological models for the gain broadening and identify the need for enhancements. Oversimplified models for the gain might lead to misinterpretations concerning the relative importance of physical processes being involved, as adjustment of carrier transport parameters can have a similar impact on the laser characteristics as modifications of gain parameters.

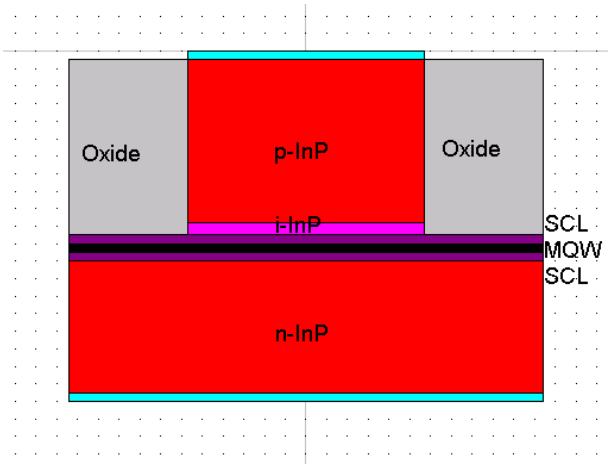

Fig. 2.2. Cross section of the ridge waveguide Fabry–Perot laser structure studied in our simulations.

2.3.1 Laser Structure

We study a multi-quantum well (MQW) ridge waveguide laser diode with a Fabry–Perot cavity, as described in detail in [11, 32]. Figure 2.2 depicts a cross section of the device. In the active region, six compressively strained $\mathrm{In}_x\mathrm{Ga}_{1-x}\mathrm{As}_y\mathrm{P}_{1-y}$ quantum wells with nominal composition $x = 0.76$ and $y = 0.79$ and a thickness of 6.4 nm are embedded in 5-nm-thick barriers made of $\mathrm{In}_{0.71}\mathrm{Ga}_{0.29}\mathrm{As}_{0.55}\mathrm{P}_{0.45}$. The multi-quantum well region is sandwiched between two undoped $\mathrm{In}_{0.171}\mathrm{Ga}_{0.829}\mathrm{As}_{0.374}\mathrm{P}_{0.626}$ separate confinement layers (SCLs). The cladding layers are made of InP. On the p-side of the structure the first 0.14 μm are undoped to avoid diffusion of acceptors into the active layers. The acceptor concentration is $4 \times 10^{17}\mathrm{cm}^{-3}$ within the p-InP cladding layer. In the n-type cladding layer, the donor concentration is $8 \times 10^{17}\mathrm{cm}^{-3}$. The p-type cladding layer is etched down to the separate confinement to leave a 57 μm-wide ridge forming the lateral mode confinement. The cleaved facets have a reflectivity of $R = 0.28$ and the cavity length is 269 μm. Figure 2.3 shows conduction and valence band within the regions surrounding the active layer for a vertical cut along the symmetry plane.

2.3.2 Sample Characterization

Due to the predictive capabilities of the many-body theory, comparison of measured and calculated photoluminescence spectra allows for the characterization of the sample. A methodology has been described that makes it possible to use this procedure for on-wafer testing [28, 29]. Static disorder in the quantum wells leads to an inhomogeneous broadening of optical resonances due to local fluctuations of the confinement potential. By applying

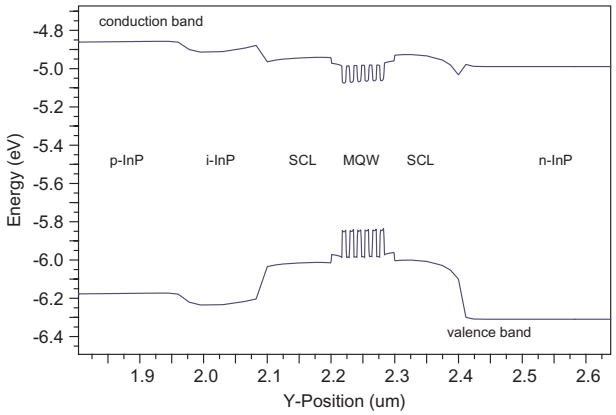

Fig. 2.3. Conduction and valence band above threshold for $T = 333$ K.

a Gaussian broadening convolution to the computed spectra, the sample quality can be assessed by fitting the experimental findings. Furthermore, comparison of the spectral position of the photoluminescence spectrum can indicate deviations of the sample geometry and material composition from the nominal specification. Temperature- and density-dependent experiments allow us to distinguish between the homogeneous collision broadening and the disorder-induced inhomogeneous broadening, because in contrast to the particle collisions, the influence of static disorder does not exhibit any dependence on temperature or carrier density.

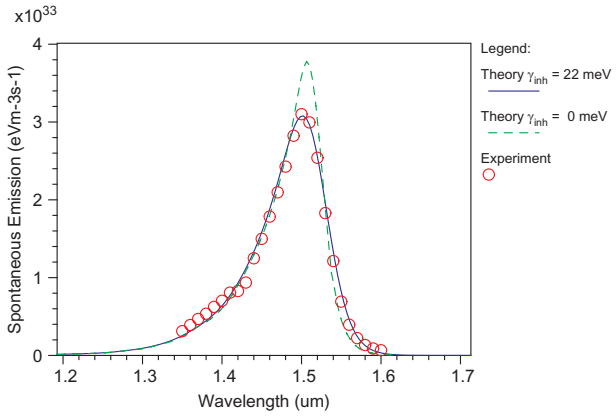

Fig. 2.4. Comparison of measured photoluminescence with calculations based on the many-body gain theory for specified inhomogeneous broadening γ_{inh} for density $N = 8.5{\times}10^{11}\mathrm{cm}^{-2}$ and temperature $T = 300$ K.

In Fig. 2.4, experimental photoluminescence is reproduced by computations based on the many-body gain theory. In order to achieve agreement, a blue shift of 23 meV with respect to the measurement had to be assumed. This indicates a slight deviation of the material composition from the nominal values. A 3% reduction of the Indium or Arsenic concentration would lead to such a shift. Assuming the nominal concentrations are correct, a deviation of the well width by 1 nm from the nominal value would also explain the shift. Such a deviation seems very unlikely because the growth process can be controlled to a good degree in this regard. Therefore, we proceed assuming $x = 0.745$ and $y = 0.775$. The nominal material composition, as specified in [11, 32], is based on an analysis of the photoluminescence and strain using a simpler theory and bowing parameters for the bulk material band gap different from those used here, which explains the deviations in the resulting material composition [46].

For determining the inhomogeneous broadening, a series of density-dependent photoluminescence spectra would be desirable to distinguish carrier-collision-induced homogeneous broadening from disorder-induced inhomogeneous broadening. However, the carrier density dependence of the lineshape helps to determine the inhomogeneous broadening to be approximately 22 meV using only one experimental photoluminescence spectrum at low carrier density. Note that this sample characterization should not be regarded solely as a parameter calibration step, as in return, it allows for the identification of deviations from the nominal geometry and composition, and it helps to assess the quality of the growth process.

2.3.3 Gain Spectra

Figure 2.5 shows gain spectra for different temperatures and carrier densities obtained using a free-carrier model [left column, Fig. 2.5(a) and (b)] in comparison with the results of the microscopic many-body theory [right column, Fig. 2.5(c) and (d)] [48]. The upper row [Fig. 2.5(a) and (c)] depicts gain spectra for increasing carrier density, while the lower row [Fig. 2.5(b) and (d)] shows gain spectra for increasing temperature. For further illustration, Fig. 2.6 depicts the peak gain obtained using the free-carrier model in comparison with computations based on the many-body theory as a function of the carrier density for different temperatures. The gain spectra obtained using the two models exhibit significant differences in amplitude and overall spectral shape as a consequence of interactions, which are neglected in the simpler free-carrier approach but included in the many-body theory.

In the absorptive regime, the attractive part of the Coulomb interaction leads to formation of excitons leading to a distinct resonance below the bandedge [Fig. 2.5(c)], which is missing in the free-carrier model spectra. Above the bandedge, Coulomb enhancement effects influence the spectral shape of the absorption due to excitonic continuum states. For higher density, the excitonic resonance disappears. However, excitonic correlations persist leading

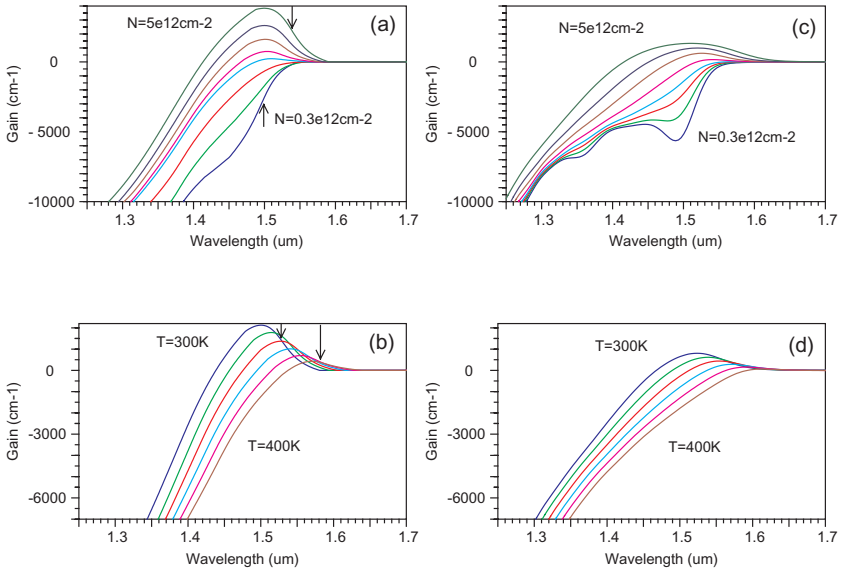

Fig. 2.5. Gain spectra computed using the free-carrier model are shown in (a) and (b) and gain spectra based on the many-body gain theory are shown in (c) and (d). (a,c): for increasing carrier density $N = 0.3/0.6/0.9/1.2/1.7/2.5/3.5/5.0\times10^{12}\text{cm}^{-2}$ at $T = 300$ K. (b,d): for increasing temperature $T = 300/320/340/360/380/400$ K at $N = 3.0 \times 10^{12}\text{cm}^{-2}$. The arrows in (a) and (b) indicate the energetic position of the lowest optical transition for the lowest and highest density in (a) and for the lowest and highest temperature in (b).

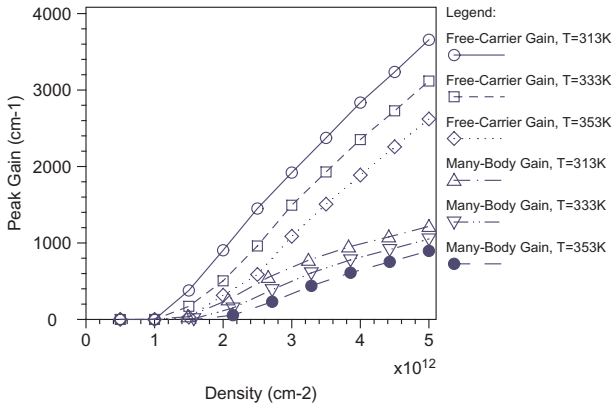

Fig. 2.6. Peak material gain as a function of quantum well carrier density for different temperatures. Results obtained using the free-carrier gain model are compared with calculations based on the many-body theory.

to a red-shift of the gain/absorption with respect to the material band gap in addition to carrier-induced band gap renormalizations. By adjusting the optical band gap, an error of the order of an excitonic binding energy can be corrected in the simpler free-carrier model for the gain regime. However, it is still unable to predict the position accurately and requires experimental data to calibrate the spectrum. Although band gap renormalizations are a consequence of microscopically including the Coulomb interaction in the many-body theory, the free-carrier approach accounts for the decrease of transition energy with increasing carrier density by applying a phenomenological band gap reduction, which is based on the local density approximation for the carrier Coulomb self-energies [47]. The resulting energetic position of the lowest subband transition is indicated by arrows in Fig. 2.5 for the lowest and the highest carrier density. In spite of the density-induced band gap reduction, both models predict a blue-shift of the gain peak for increasing density due to higher subband contributions overcompensating band gap renormalizations. This blue-shift is stronger in the spectra computed based on the many-body theory than in the results of the free-carrier approach.

In a Fabry–Perot cavity of common resonator length of several hundred micron, a quasi-continuum of longitudinal modes is available. Spectral shifts might lead to inaccuracies in predicting the laser frequency, but they have limited impact on the output characteristics, as a resonator mode close to the gain peak can always be found. Although spectral details have minor influence on the characteristics of a Fabry–Perot laser, it becomes more significant in cavities with a strong optical confinement such as in vertical-cavity surface-emitting lasers (VCSELs) An error on the order of an excitonic binding energy can shift the spectral region of maximum gain into the reflection band of the cavity. Furthermore, in such structures, spectral details around the transparency point can be important. In our example, the macroscopic results, such as light-current characteristics, depend on the gain peak, but they are insensitive to the rest of these spectral details. The position of the gain maximum determines the lasing modes and, therefore, the emission wavelength. The threshold current density and the slope efficiency are affected by the magnitude of the gain and its density and temperature dependence. Carrier–phonon and carrier–carrier scattering induce broadening, and subsequently reduce the peak amplitude of the gain. As these interactions are included in the microscopic theory within the Markovian limit, the temperature- and density-dependent broadening and, therefore, the total magnitude of the gain can be predicted as a function of the injection current.

Due to carrier–carrier scattering-induced broadening, the increase of gain with increasing density shows a stronger saturation behavior than the gain spectra obtained by neglecting these effects in the free-carrier approach, as can be seen from Fig. 2.5(a) and (c) and Fig. 2.6. Lower differential gain and stronger saturation behavior of the peak gain for increasing carrier concentration can be observed for the many-body gain compared with the free-carrier

model. In the free-carrier model, a linewidth broadening parameter has to be specified to phenomenologically account for carrier–carrier and carrier–phonon interactions [see (2.33)], which prohibits the model from predicting the absolute gain amplitude and requires calibration using experimental data. We use a linewidth broadening of 26 meV for the gain spectra shown in Fig. 2.5. Comparing the gain amplitude of the free-carrier model with the many-body gain spectra (see Fig. 2.6), the broadening parameter would have to be increased to reduce the gain peak and differential gain to the correct values as given by the many-body gain. However, for increased broadening, the deviation of the free-carrier gain from the many-body gain around the transparency density would increase.

Naturally, the complex details of the carrier–carrier and carrier–phonon scattering processes cannot be included in one number. Therefore, the linewidth broadening can be adjusted to reproduce the gain amplitude of experiments only in a narrow window of carrier densities. The effective decay time approach fails to describe the behavior over a wider range of densities or temperatures, as discussed in Chap. 1. Improving the model for more complex lineshapes or introducing a density and temperature dependence would add fit parameters. Although experimental results can be reproduced, additional effort in model calibration has to be invested.

For a constant linewidth broadening parameter, we observe a weaker temperature dependence of the free-carrier gain [Fig. 2.5(b)] compared with the results obtained by the many-body theory [Fig. 2.5(d)]. Although a quantitative change of the gain amplitude is observed for the free-carrier model, the gain computed based on the many-body theory is almost completely suppressed by increasing the temperature from 300 K to 400 K for constant carrier density. The temperature dependence of the free-carrier gain is implicitly determined by the temperature dependence of the carrier distribution functions [see (2.31)]. In addition to the inversion factor, the many-body gain shows the influence of the increased phonon scattering for higher temperatures. A red-shift of the gain with increasing temperature is predicted by both models and is caused by band gap narrowing. The energetic position of the lowest subband transition is indicated by arrows in Fig. 2.5(b) for the lowest and highest temperature.

2.3.4 Light-Current Characteristics and Model Calibration

In Figs. 2.7 and 2.8, light-current curves obtained by the free-carrier model and the many-body model (lines) are compared with measured data (denoted by symbols) for the structure described in Sect. 2.3.1. The laser structure and experimental data have been taken from [32]. The experiments were performed under pulsed conditions to avoid self-heating. Therefore, a uniform temperature distribution, as given by the stage temperature, can be assumed. Both models can reproduce the experimental findings after model calibration.

With known gain spectrum calculated using the many-body theory, the calibration of remaining transport model parameters is greatly simplified due to a significant reduction of the parameter space. Aside from the gain, the spontaneous recombination is completely determined, as well as refractive index changes within the active layer. The use of simpler gain models requires simultaneous adjustments of transport and gain model parameters to account for density and temperature dependence of experimental findings.

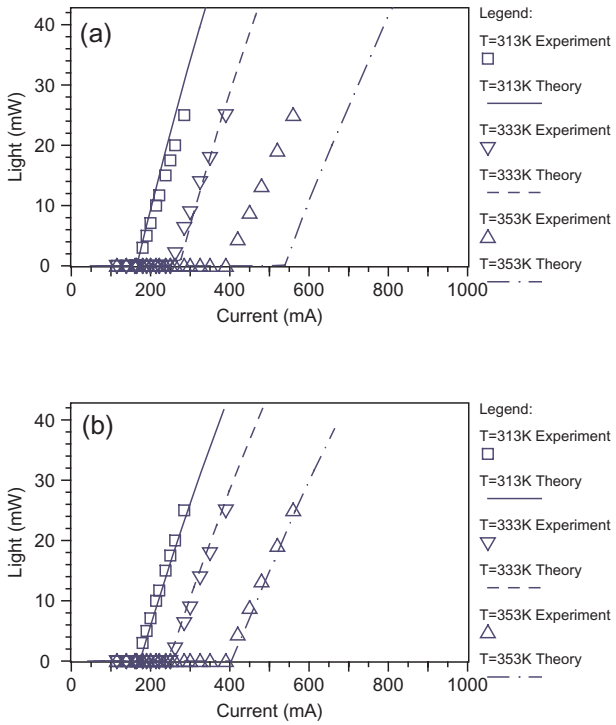

Fig. 2.7. Light-current characteristics for increasing temperature using the many-body gain model in comparison with experimental data. (a): Prediction based on default parameters of the simulator. (b): Calibrated result.

The uncalibrated simulation results obtained for each model, using default parameters from the material library of our simulator, show that the prediction based on the many-body theory is much closer to the experimental findings, concerning threshold current and slope efficiency, than the prediction based on the free-carrier approach [denoted by "default parameters" in Fig. 2.8(a)]. The free-carrier model predicts a lower threshold current and a much smaller shift of the threshold as a function of temperature. The slope efficiency is higher for the free-carrier approach than the microscopic many-body calculation, which agrees well with the experimental data. The weaker

temperature sensitivity of the free-carrier model-based prediction is based on the weaker temperature dependence of the gain due to neglecting the electron–phonon interaction, as observed in Fig. 2.5. Furthermore, as a consequence of not accounting for carrier–carrier and carrier–phonon collision effects, the total amplitude of the gain as well as the differential gain is higher for the free-carrier model compared with the many-body gain theory (see Fig. 2.5), leading to lower threshold of the light-current characteristic and influencing the slope efficiency.

Besides the gain, nonradiative recombination affects the threshold current density and slope efficiency. Auger recombination, Shockley–Read–Hall recombination, and spontaneous emission into nonlasing modes decrease the carrier densities in the active layers without contributing to light amplification. Waveguide and background absorptive losses, intervalence band absorption, and lateral leakage are other processes affecting the device behavior. The Auger recombination, in particular, has been pointed out as one of the dominating processes [32, 39]. Within the nonradiative recombination mechanisms, it has the strongest density dependence, being cubic, whereas other recombination mechanisms such as spontaneous recombination and Shockley–Read–Hall processes have a weaker, quadratic and linear density dependence, respectively [see (2.9), (2.14), (2.10)]. As a decrease of gain with increasing temperature has to be compensated by an increase of carrier density within the active layers, the threshold injection current increases with temperature. The efficiency of the injection is affected by the dark recombination, which acts to reduce the carrier density. Due to the nonlinearity with respect to the carrier density dependence, the Auger recombination tends to strongly amplify the effects of the temperature-dependent gain reduction, leading to further reduction of slope efficiency and increase of threshold currents. This mechanism scales with the Auger coefficients. The same argument applies to a lesser degree to other carrier-dependent processes involved in the coupled problem of carrier transport and radiative interaction, as an increase in temperature will indirectly increase the carrier density in the quantum wells. Note that the strong decrease of the differential gain with increasing carrier density observed for the many-body gain tends to nonlinearly increase the carrier densities required to compensate a temperature-induced reduction of the gain, thus enhancing the temperature sensitivity.

As the gain is completely determined by the microscopic calculation, only transport parameters have to be adjusted to fit the measurement. Due to the prediction overestimating the temperature dependence in Fig. 2.7(a), we reduce the Auger coefficients to $C_e^{Auger} = 1 \times 10^{-31}\mathrm{cm}^6\mathrm{s}^{-1}$, $\mathrm{C_h^{Auger}} = 5 \times 10^{-31}\mathrm{cm}^6\mathrm{s}^{-1}$ and compensate with a decrease of the carrier lifetime in the Shockley–Read–Hall recombination within the quantum wells: $\tau_e^{SRH} = 5\times10^{-9}\mathrm{s}$, $\tau_\mathrm{h}^\mathrm{SRH} = 5\times10^{-8}\mathrm{s}$. We slightly reduce the carrier-dependent loss and increase carrier-independent contributions. Based on the photoluminescence comparison, an inhomogeneous broadening of 22 meV is used. A good match

of the experimental curves can be obtained using one set of transport model parameters for all temperatures (see Table 2.2).

Table 2.2. Material and Model Parameters Used for the Active Layers. Default Parameters of the Simulator, Parameters Calibrated Using the Many-body Gain Model, and Parameters Published in [32] are Listed.

Parameter	Default	Calibration	[32]
τ_e^{SRH}/s	2.44e-8	5.e-9	2.e-8
τ_h^{SRH}/s	2.88e-6	5.e-8	2.e-8
$B/(\mathrm{cm}^3\mathrm{s}^{-1})$	2.26e-10	1.2e-10	1.2e-10
$C_e^{Auger}/(\mathrm{cm}^6\mathrm{s}^{-1})$	4.43e-31	1.0e-31	0.0
$C_h^{Auger}/(\mathrm{cm}^6\mathrm{s}^{-1})$	3.95e-30	5.0e-31	1.6e-28
$E_e^{Auger,act}$/meV	0.0	0.0	60
$E_h^{Auger,act}$/meV	0.0	0.0	0.0
$\alpha_0/(\mathrm{cm}^{-1})$	0.0	16.0	0.0
k_e^{fca}/cm^2	1.e-18	1.0e-18	1.0e-18
k_h^{fca}/cm^2	2.e-17	1.8e-17	8.2e-17
γ_0/meV (only free-carrier gain)	26	120/190/265	41
γ_{inh}/meV (only many-body gain)	0.0	22.0	–

Based on our advanced treatment of the gain, we find that the influence of the Auger recombination on the temperature dependence of InGaAsP quantum well lasers is secondary. Our Auger parameters used in our calibrated simulations are about one to two orders of magnitude lower than parameters published in the literature for InGaAsP [11]. The large spread of values in the literature indicates that the Auger process in quantum wells deserves further scientific investigation. Experimentally, Auger coefficients are often determined as the coefficient of the cubic term in a polynomial fit of a density-dependent measurement. Other processes could contribute to the measured coefficient leading to an overestimation of the Auger recombination. Theoretical Auger parameters found in [49, 50] for unstrained InGaAsP quantum wells are in good qualitative agreement with our findings. The influence of 1% strain present in our quantum well structure should be negligible compared with the general uncertainty associated with Auger recombination for this material system. It has been suggested that strain could be used to reduce the Auger recombination in InGaAsP quantum wells [40, 51]. Note that parameters for quantum well Auger recombination can deviate significantly from coefficients known for bulk material. Moreover, for narrow quantum wells, thresholdless and quasi-threshold Auger processes with weak temperature dependence dominate over threshold Auger processes present in the bulk limit, which are characterized by a higher activation energy [50]. Our simulations indicate that the gain reduction, due to carrier–phonon and carrier–carrier scattering-induced dephasing, primarily determines the temperature sensi-

tivity of this material system for the temperature range reasonable for laser applications investigated here. For even higher temperatures, it can be expected that the cubic density dependence of the Auger process will increase its relative importance due to the implicit increase of density with temperature. Furthermore, vertical carrier leakage out of the active region becomes more important [32, 52].

The role of nonradiative recombination and gain in this context has been discussed in the literature [39, 40, 45]. In particular, the influence of the reduction of differential gain with increasing temperature has been discussed in experimental investigations of the temperature sensitivity [40, 45]. The decrease of differential gain with temperature is consistent with our findings, as, in order to sustain lasing operation, the effects of the increased temperature will be compensated by an increase of carrier density, implying a collision-induced decrease in differential gain, as can be seen from the saturation behavior of the gain spectra as a function of carrier density in Fig. 2.5(c).

Pointing out the significance of the gain in determining the temperature sensitivity, Piprek et al. required higher Auger parameters than used here to reproduce their experimental data for constant gain broadening [32]. Following their calibration procedure, we obtain a good fit to the experimental findings using the free-carrier gain approach with constant broadening parameter in connection with increased Auger recombination for similar model parameters, as is shown in Fig. 2.8(a) (denoted by "published calibrated parameters"). We use Auger parameters of $C_e^{Auger} = 0$, $C_h^{Auger} = 1.1 \times 10^{-28}$ and $E_h^{Auger,act} = 80$ meV. Comparison of this fit with the result computed using our lower default parameters demonstrates the influence of the Auger recombination on the temperature sensitivity. Our low default Auger parameters ($C_e^{Auger} = 4.43 \times 10^{-31}\mathrm{cm^6s^{-1}}$, $\mathrm{C_h^{Auger}} = 3.95 \times 10^{-30}\mathrm{cm^6s^{-1}}$) explain the weak temperature dependence of the results obtained in the uncalibrated prediction using the free-carrier gain model. Moreover, temperature independent Auger coefficients were used [$E_{e/h}^{Auger,act} = 0$ in (2.11)]. The temperature sensitivity observed in the light-current characteristic for the low default Auger parameters is more directly related to the weak dependence observed in the gain spectra in Fig. 2.5, because the amplification effect described above is reduced with respect to the parameter set with high Auger recombination.

As our advanced model indicates the domination of collision broadening in determining the temperature sensitivity, we keep the calibrated transport model used within the computations based on the many-body theory and only switch to the free-carrier gain model. In order to obtain the fit in Fig. 2.8, we use the linewidth broadening parameter to fit the curves individually for each temperature, while keeping all other parameters unchanged. The linewidth broadening can be understood as a simplified model for dephasing due to quasi-particle scattering. However, it fails to describe the temperature and density dependence of these processes. Using increased

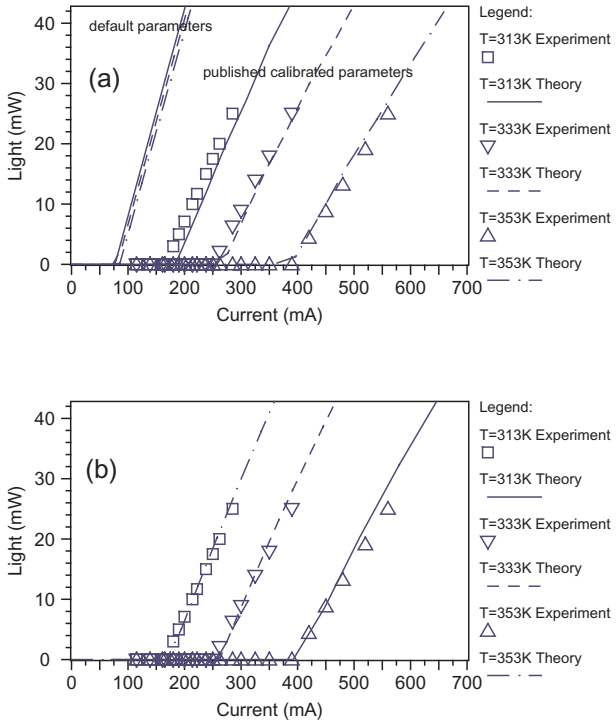

Fig. 2.8. Light-current characteristics for increasing temperature using the free-carrier gain model in comparison with experimental data. (a): Prediction based on default parameters and calibration based on Auger recombination parameters from [32]. (b): Calibration based on parameters obtained using the many-body gain model.

linewidth broadening parameters with increasing temperature, the threshold current can be adjusted to match the experimental data as shown in Fig. 2.8. The slope efficiency of the fitted simulation results tends to be slightly higher in the simulation compared with the experiment, especially for higher temperatures. As the simple broadening model cannot capture the complex dynamics of carrier–carrier scattering, the density dependence is not taken into account correctly. As the density will increase to compensate for the effects of the increased temperature, the more linear differential gain of the free-carrier model will cause stronger discrepancies with respect to the carrier-collision-induced decrease of differential gain. Furthermore, the broadening is uniformly applied to the full range of subband transitions instead of having an energy dependence according to the spectrally resolved carrier densities. As a significant reduction of gain requires a strong increase of the uniform broadening, unphysically high fit parameters are obtained (120/190/265 meV for 313/333/353 K), which should not be interpreted in terms of a directly

associated scattering mechanism. Introducing proper dependencies with respect to density, temperature, and energy, the linewidth broadening model could be improved. However, new model parameters would be increasing the effort for calibration. In spite of the shortcomings of the linewidth broadening model, we have demonstrated that it provides an alternative method to the increase of Auger recombination for reproducing the experimental data using a free-carrier approach, which is in agreement with our findings from the advanced treatment of the gain.

Without detailed knowledge of the gain spectrum of a given material, ambiguities between different processes determining the temperature and density dependence of the light output characteristics can exist. A good fit can be obtained by calibrating transport parameters only, indicating a correct description of the underlying physics. Auger recombination has been regarded as the dominant mechanism determining the temperature sensitivity of InGaAsP lasers in the past. As our investigation indicates, this conclusion was based on the use of oversimplified gain models leading to an overestimation of the Auger recombination. In order to avoid these ambiguities, a calibration procedure should attempt to calibrate the gain spectrum first. Density- and temperature-dependent photoluminescence measurements could help in determining broadening parameters describing density and temperature dependence of the gain. Using gain and photoluminescence spectra based on the microscopic many-body theory, this step is already completed. Additional benefit is provided by sample characterization. After the gain and spontaneous emission are calibrated, the remaining transport parameters can be adjusted by performing full-scale laser simulations.

2.3.5 Self-Heating

In Fig. 2.9, light-current characteristics (a) and the corresponding maximum lattice temperature within the device (b) are shown for calculations involving the heat flow equation (2.15) in comparison with results based on a uniform temperature distribution. The many-body gain model was used for these computations. Different boundary conditions can be imposed at the metal contacts. At the top contact on the p-type side of the device, a reflective boundary is assumed leading to vanishing heat flux. A lumped thermal resistor that describes the heat conductance of the substrate and the heat sink is associated with the bottom electrode. For ideal cooling of the laser, corresponding to vanishing lumped thermal resistance in our example, the temperature at the thermal contact is forced to the external stage temperature described by imposing a Dirichlet boundary condition. The more realistic boundary condition (2.23) with finite thermal conductance associated with the contact accounts for the thermal properties of regions that are not included in the simulation domain, such as substrate, mounting, or packaging [35].

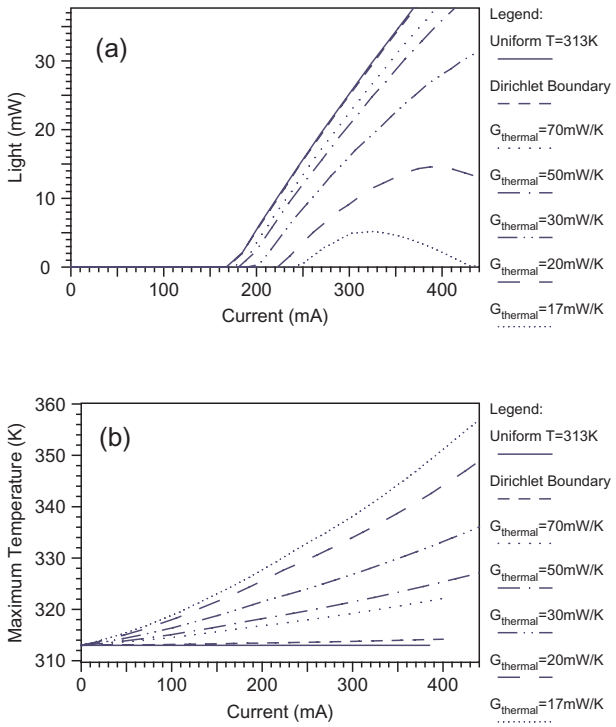

Fig. 2.9. Light-current characteristics for increasing temperature using the many-body gain model for different boundary conditions for the heat flow equation: Uniform temperature distribution with $T = 313$ K, Dirichlet boundary condition forcing $T = 313$ K at the contacts, lumped thermal conductance associated with the bottom contact with given thermal conductance $G_{thermal}$.

For the Dirichlet boundary condition, we observe negligible effect on the light-current characteristic. As can be seen from Fig. 2.9(b), the maximum temperature increases by only 2 K with respect to the stage temperature of $T_C = 313$ K. By applying a finite thermal conductance, the local temperature at the thermal contact, and therefore within the device, is allowed to rise. Higher temperatures are reached within the device as shown in Fig. 2.9(b) for decreasing thermal conductance $G_{thermal}$ associated with the bottom electrode, describing less-efficient cooling of the laser. As a consequence, an increase in threshold current and a decrease in slope efficiency with respect to the isothermal case can be observed. Furthermore, the light-current curves show the characteristic thermal roll-off. For thermal conductivities $G_{thermal} < 15$ mW/K, lasing is completely suppressed at stage temperature $T_C = 313$ K due to self-heating effects. As our findings from Sect. 2.3.4 indicate, the temperature-induced reduction of the gain is the primary cause of these thermal effects. As can be seen from Fig. 2.10, the maximum tempera-

ture occurs in the p-type ridge and decreases across the active layers toward the heat sink at the bottom contact. The heat is generated dominantly due to Joule heat around the quantum wells and the p-type layers as well as recombination heat around the active region. The lattice heat equation was deactivated in the oxide regions (see Fig. 2.2), thus keeping the temperature equal to the ambient temperature in those regions.

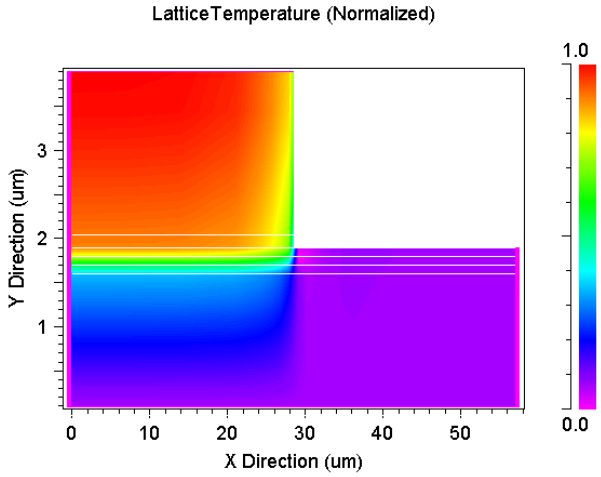

Fig. 2.10. Temperature profile of the half-domain ridge-waveguide laser structure as obtained by solving the heat flow equation.

Figure 2.11 shows a comparison of the effects of self-heating obtained using the many-body gain compared with the free-carrier gain model. For the many-body gain, strong self-heating effects can be observed in the light-current characteristic caused by quasi-particle interaction-induced gain broadening. Calculations based on the free-carrier model with the same parameter settings, in particular, the low Auger parameters obtained by our calibration procedure, show very weak influence of the temperature increase (indicated by "Free-Carrier Gain A" in Fig. 2.11). In contrast to the temperature and carrier density dependence of the collision broadening included in the many-body theory, the gain broadening of the free-carrier model is constant. Weaker effects of the self-heating-induced temperature increase are observed compared with the computations using the advanced gain model. This result was expected from the weak temperature sensitivity observed for the uniform temperature simulations for our low default Auger parameters [see Fig. 2.8(a)]. Moreover, our calibrated Auger coefficients are even lower (see Table

2.2). Although it is possible to adjust the constant gain broadening for the isothermal case, the self-heating simulation demonstrates the shortcoming of a missing temperature and carrier density dependence of the broadening because the temperature varies spatially and with the bias conditions. Using the higher Auger parameters from [32] for this structure, the influence of self-heating leads to considerable increase of threshold and decrease of slope efficiency with respect to the uniform temperature case, as the strong carrier density dependence of the Auger recombination tends to amplify the effects of the temperature-induced gain reduction aside from its explicit exponential temperature dependence (see Fig. 2.11(a) "Free-Carrier Gain B").

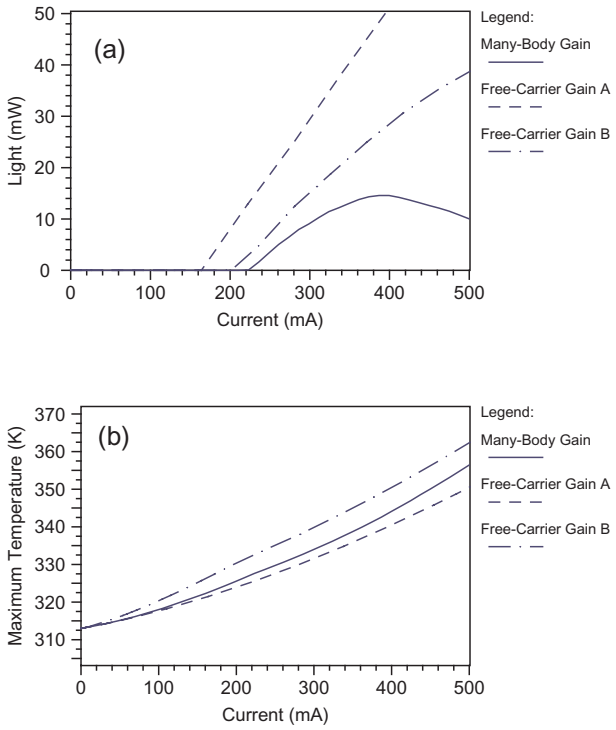

Fig. 2.11. Light-current characteristics for stage temperature $T = 313$ K using the many-body gain compared with results obtained for the free-carrier model for parameters calibrated based on the many-body calculations (Free-Carrier Gain A) and for calibrated parameters taken from [32] (Free-Carrier Gain B).

Figure 2.11(b) depicts the maximum temperature within the device occurring during the respective simulations. As can be seen from Fig. 2.10, the maximum occurs in the vicinity of the active layer; thus, it roughly indicates the local temperature influencing the optical transitions. For all of the three model settings, similar temperatures occur in the device. Slightly higher tem-

peratures are reached for the high Auger recombination parameter settings ("Free-Carrier Model B") compared with the lower Auger parameters obtained by the calibration based on the many-body gain models ("Many-Body Gain", "Free-Carrier Gain A") as the higher Auger recombination implies higher contributions to the recombination heat source.

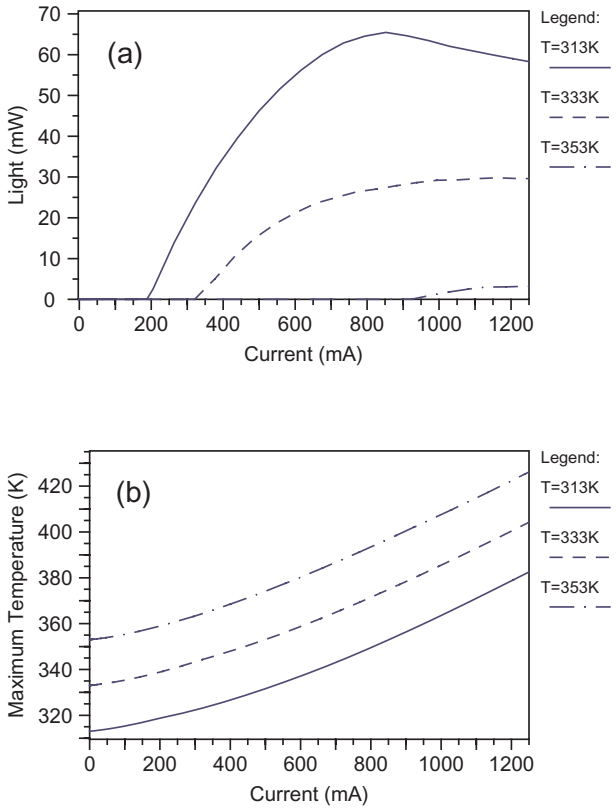

Fig. 2.12. (a): Light-current characteristics for increasing stage temperature T using the many-body gain model and including self-heating, (b): corresponding maximum temperature within the device.

In self-heating simulations, modeling the correct temperature dependence of the gain broadening cannot be avoided in order to obtain reliable results, as can be seen from Fig. 2.11. The effective decay time approximation can reproduce the gain spectra for a narrow window of carrier densities and temperatures as discussed in Sect. 2.3.3 and in Chapt. 1. For isothermal full-scale laser simulations, experimental light-current characteristics can be reproduced once parameters are calibrated, as the increase of carrier density above the lasing threshold is weak and the temperature is kept constant.

However, in self-heating simulations, the temperature varies spatially and as a function of the injection current. Temperature-induced gain reductions imply a compensating increase of the carrier concentrations. The increased range of variation in carrier density and temperature cannot be covered by the constant linewidth broadening. Therefore, the self-heating results obtained using the free-carrier model differ strongly from the advanced many-body computations (see Fig. 2.11), in spite of the agreement between the light-current characteristics computed using the respective models with the same parameters for isothermal conditions (see Figs. 2.7(b), 2.8(b) and 2.8(a) "published calibrated parameters").

In Fig. 2.12, simulation results are shown for increasing stage temperature. The many-body gain model was used for these calculations. The thermal conductance associated with the heat sink at the bottom electrode was set to $G_{thermal} = 45$ mW/K. As can be seen by comparing these light-current characteristics [Fig. 2.12(a)] with Fig. 2.7(b), temperature effects are stronger under self-heating conditions. A uniform temperature distribution can be prepared experimentally by pulsed operation, where the bias is applied only for a short period of time during one duty cycle. In this mode of operation, the heat generated within the device can be dissipated to the environment efficiently, whereas during the short lasing period, the heat capacity of the device prevents significant increase of the temperature [see left-hand side of (2.15)]. This situation is desirable from an experimental point of view, because it eliminates self-heating effects and eases analysis of the dominant physical mechanisms influencing the performance of the device. However, in most applications, diode lasers are operated under CW conditions. In this mode of operation, a steady state between heating within the device due to transport and recombination processes and external cooling will occur. A significant increase of the temperature with respect to the stage temperature will occur in the active layer, as can be seen from Fig. 2.12(b). The theoretical description of such a situation requires the coupled solution of carrier and thermal transport as well as radiative interaction with the light field.

2.4 Summary

We have demonstrated the integration of advanced gain modeling based on a microscopic many-body theory into full-scale laser simulations. Our approach has been applied to the investigation of the temperature sensitivity of InGaAsP quantum well lasers. It has been shown that the gain broadening due to carrier–carrier and carrier–phonon scattering-induced dephasing dominantly determines the temperature sensitivity of these laser structures rather than nonradiative recombination.

Our microscopic gain model allows for an accurate prediction of the gain spectrum for a specific material system based solely on material parameters. The energetic position and the collision broadening of the gain maximum have

a significant impact on the optical properties of Fabry–Perot laser diodes, in particular, emission wavelength, threshold current, and slope efficiency, as discussed here. The detailed spectral behavior of the gain can be expected to be of more importance for advanced structures like VCSELs, which exhibit a strong optical confinement in the longitudinal direction.

The advanced many-body gain theory has been compared with the free-carrier gain model, which is a common approach in commercial laser simulators. The advantage of the predictive modeling of the gain by the microscopic many-body theory with respect to simpler models carries over to the full-scale laser simulation. Calibration effort can be reduced while improving the overall predictive capabilities of the simulation. In order to improve the free-carrier approach, density, temperature, and energy dependences would have to be added to the gain broadening model to describe effects of carrier–carrier and carrier–phonon scattering phenomenologically. We suggest a calibration procedure that determines the gain model parameters first by performing optical experiments in order to avoid ambiguities between transport and gain models in describing temperature and density dependence of the overall laser performance. Using the microscopic many-body theory, this additional calibration step can be avoided.

Acknowledgment

We thank J. Piprek for valuable discussions and for providing experimental data. The Tucson effort is supported by a grant from the U.S. Air Force Office for Scientific Research under grant number: AFOSR F49620-01-1-0380. The Marburg research is supported by the Max Planck Research Prize.

References

1. M. Grupen and K. Hess: IEEE J. Quantum Electron. **34**, 120 (1998)
2. B. Grote, E. K. Heller, R. Scarmozzino, J. Hader, J. V. Moloney, and S. W. Koch: Integration of microscopic gain modeling into a commercial laser simulation environment. In: *Physics and Simulation of Optoelectronic Devices XI* Proc. SPIE, vol. 4986, ed by M. Osinski, H. Amano, and P. Blood, pp. 413-422 (2003)
3. W. Van Roosbroeck: Bell System Tech. J. **29**, 560 (1950)
4. D. L. Scharfetter and H. K. Gummel: IEEE Trans. Electron Devices **ED-16**, 64 (1969)
5. K. Blotekjaer: IEEE Trans. Electron Devices **ED-17**, 38 (1970)
6. R. K. Cook and J. Frey: COMPEL **1**, 65 (1982)
7. D. Chen, E. C. Kan, U. Ravaioli, C. W. Shu, and R. W. Dutton: IEEE Electron Device Lette. **EDL-13**, 26 (1992)
8. D. Chen, Z. Yu, K. C. Wu, R. Goossens, and R. W. Dutton: Dual Energy Transport Model with Coupled Lattice and Carrier Temperatures. In: Proceedings 5th SISDEP Conference Vienna, Austria, pp. 157-160 (1993)

9. G. Wachutka: IEEE Trans. on Computer-Aided Design **CAD-9**, 1141 (1990)
10. S. Selberherr: *Analysis and Simulation of Semiconductor Devices* (Springer Verlag, New York 1984)
11. J. Piprek: *Semiconductor Optoelectronic Devices* (Academic Press, San Diego 2003)
12. G. Wachutka: COMPEL **10**, 311 (1991)
13. H. Brand: Thermoelektrizität und Hydrodynamik. Dissertation, Technical University Vienna, Austria (1994) (ohttp://www.iue.tuwien.ac.at/phd /brand/diss.html)
14. M. A. Alam, M. S. Hybertsen, R. K. Smith, and G. A. Baraff: IEEE Trans. Electron Devices **47**, 1917 (2000)
15. J. Luttinger and W. Kohn: Phys. Rev. **97**, 869 (1955)
16. G. L. Bir and G. E. Pikus, eds.: *Symmetry and Strain-induced Effects in Semiconductors* (Wiley, New York 1974)
17. C. Hermann and C. Weisbuch,: Phys. Rev. B **15**, 823 (1977)
18. E. O. Kane: Energy band theory. In: *Handbook on Semiconductors* ed. by T. S. Moss (North-Holland, New York 1982) PP. 193–217
19. S. L. Chuang: Phys. Rev. B **43**, 9649 (1991)
20. P. von Allmen: Phys. Rev. B **46**, 15382 (1992)
21. M. S. Hybertsen, G. A. Baraff, S. K. Sputz, D. A. Ackermann, G. E. Shtengel, J. M. Vandenberg, and R. Lum: Modeling of optical spectra for characterization of multi-quantum well InGaAsP-based lasers. In: *Physics and Simulation of Optoelectronic Devices IV* Proc. SPIE, vol. 2693, ed. by W. W. Chow and M. Osinski, pp. 430-441 (1996)
22. F. Oyafuso, P. von Allmen, M. Grupen, and K. Hess: Gain calculation in a quantum well simulator using an eight band $\mathbf{k} \cdot \mathbf{p}$ model. In: *Proc. 4th Int. Workshop Computat. Electron.* (Tempe, AZ 1995)
23. B. Zee: IEEE J. Quantum Electron. **QE-14**, 727 (1978)
24. M. Yamada and Y. Suematsu: J. Appl. Phys. **52**, 2653 (1981)
25. W. W. Chow and S. W. Koch: *Semiconductor-Laser Fundamentals: Physics of the Gain Materials* (Springer, Berlin 1999)
26. H. Haug and S. W. Koch: *Quantum Theory of the Optical and Electronic Properties of Semiconductors*, 3rd edn (World Scientific, Singapore 1994)
27. J. Hader, J. V. Moloney, S. W. Koch, and W. W. Chow: IEEE J. Sel. Topics in Quantum Electron. **9**, 688 (2003)
28. J. Hader, A. R. Zakharian, J. V. Moloney, T. R. Nelson, W. J. Siskaninetz, J. F. Ehret, K. Hantke, S. W. Koch, and M. Hofmann: Optics and Photonics News **13 (12)**, 22 (2002)
29. J. Hader, A. R. Zakharian, J. V. Moloney, T. R. Nelson, W. J. Siskaninetz, J. F. Ehret, K. Hantke, M. Hofmann, and S. W. Koch: IEEE Photon. Technol. Lett., **14**, 762 (2002)
30. M. Grupen, K. Hess, and G. H. Song: Simulation of transport over heterojunctions. In: *Proc. 4th Int. Conf. Simul. Semicon. Dev. Process.*, vol 4, pp. 303-311 (Zurich, Switzerland 1991)
31. S. Seki, W. W. Lui, and K. Yokoyama: Appl. Phys. Lett. **66**, 3093 (1995)
32. J. Piprek, P. Abraham, and J. E. Bowers: IEEE Journal of Quantum Electron. **36**, 366 (2000)
33. Z. Yu, D. Chen, L. So, and R. W. Dutton: *PISCES-2ET and Its Application Subsystems*, Manual, Stanford University, Stanford, California (1994)

34. R. Thalhammer: Internal Laser Probing Techniques for Power Devices: Analysis, Modeling, and Simulation. Dissertation, Technical University Munich, Germany (2000) (http://tumb1.biblio.tu-muenchen.de/publ/diss/ei/2000/thalhammer.pdf)
35. T. Grasser and S. Selberherr: IEEE Trans. on Electron Devices **48**, 1421 (2001)
36. J. Hader, S. W. Koch, and J. V. Moloney: Sol. Stat. Electron. **47**, 513 (2003)
37. W. Chow, M. Kira, and S. W. Koch: Phys. Rev. B **60**, 1947 (1999)
38. G. P. Agrawal and N. K. Dutta: *Semiconductor Lasers* (Van Nostrand Reinhold, New York 1993)
39. J. Braithwaite, M. Silver, V. A. Wilkinson, E. P. O'Reilly, and A. R. Adams: Appl. Phys. Lett. **67**, 3546 (1995)
40. Y. Zou, J. S. Osinski, P. Grodzinski, P. D. Dapkus, W. C. Rideout, W. F. Sharfin, J. Schlafer, and F. D. Crawford: IEEE J. Quantum Electron. **29**, 1565 (1993)
41. J. Piprek, D. Babic, and J. E. Bowers: J. Appl. Phys. **81**, 3382 (1997)
42. L. J. P. Ketelsen and R. F. Kazarinov: IEEE J. Quantum Electron. **34**, 811 (1995)
43. Y. Yoshida, H. Watanabe, K. Shibata, A. Takemoto, and H. Higuchi: IEEE J. Quantum Electron. **34**, 1257 (1998)
44. A. A. Bernussi, H. Temkin, D. L. Coblentz, and R. A. Logan: Appl. Phys. Lett. **66**, 67 (1995)
45. D. A. Ackerman, G. E. Shtengel, M. S. Hybertsen, P. A. Morgan, R. F. Kazarinov, T. Tanbun-Ek, and R. A. Logan, IEEE J. Select. Topics Quantum Electron. **1**, 250 (1995)
46. J. Piprek, private communication
47. L. Hedin and B. Lundquist, *J. Phys. C* **4**, 2064 (1971)
48. Gain / refractive index / photoluminescence tables courtesy of Nonlinear Control Strategies, 1001 East Rudasill Rd., Tucson, AZ 85718
49. *New Semiconductor Materials. Characteristics and Properties*, Ioffe Physico-Technical Institute, St. Petersburg, Russia, (http://www.ioffe.ru/SVA/NSM/Semicond/)
50. A. S. Polkovnikov and G. G. Zegrya: Phys. Rev. B **58 (7)**, 4039 (1998)
51. O. Gilard, F. Lozes-Dupuy, G. Vassilieff, S. Bonnefont, P. Arguel, J. Barrau, and P. Le Jeune: J. Appl. Phys. **86(11)**, 6425 (1999)
52. J. Piprek, J. K. White, and A. J. Spring Thorpe: IEEE J. Quantum. Electron. **38**, 1253 (2002)